Remote Sensing of Environment 231 (2019) 111284

Contents lists available at ScienceDirect

Remote Sensing of Environment

journal homepage: www.elsevier.com/locate/rse

A harmonized image processing workflow using Sentinel-2/MSI and Landsat-8/OLI for mapping water clarity in optically variable lake systems

Benjamin P. Page[a,*], Leif G. Olmanson[b], Deepak R. Mishra[c]

[a] Water Resources Center, University of Minnesota, St. Paul, MN, USA
[b] Remote Sensing and Geospatial Analysis Laboratory, Department of Forest Resources, University of Minnesota, St. Paul, MN, USA
[c] Center for Geospatial Research, Department of Geography, University of Georgia, Athens, GA, USA

ARTICLE INFO

Keywords:
Water clarity
Harmonized
Atmospheric correction
Landsat-8
Sentinel-2
Lake monitoring
Lake management
Remote sensing
Validation

ABSTRACT

This study demonstrates the applicability of harmonizing Sentinel-2 MultiSpectral Imager (MSI) and Landsat-8 Operational Land Imager (OLI) satellite imagery products to enable the monitoring of inland lake water clarity in the Google Earth Engine (GEE) environment. Processing steps include (1) atmospheric correction and masking of MSI and OLI imagery, and (2) generating scene-based water clarity maps in terms of Secchi depth (SD). We adopted ocean-color based atmospheric correction theory for MSI and OLI sensors modified with associated scene-specific metadata and auxiliary datasets available in GEE to generate uniform remote sensing reflectances (R_{rs}) products over optically variable freshwater lake surfaces. MSI-R_{rs} products derived from the atmospheric correction were used as input predictors in a bootstrap forest to determine significant band combinations to predict water clarity. A SD model for MSI (SD_{MSI}) was then developed using a calibration dataset consisting of log-transformed $SD_{in\ situ}$ measurements ($\ln SD_{in\ situ}$) from 79 optically variable freshwater inland lakes collected within ± 1 day of satellite overpass on 23-Aug 2017 (MAE = 0.53 m) and validated with 276 samples collected within ± 1 day of a 12-Sep 2017 image (MAE = 0.66 m) across three ecoregions in Minnesota, USA. A separate SD model for MSI was also developed using similar spectral bands present on the OLI sensor (SD_{sOLI}) where cross-sensor performance can be evaluated during coincident overpass events. SD_{sOLI} applied to both MSI and OLI (SD_{OLI}) models were further validated using two coincident overpass sets of imagery on 27-Sep 2017 (n = 18) and 13-Aug 2018 (n = 43), yielding a range of error from 0.25 to 0.67 m. Potential sources of model errors and limitations are discussed. Data derived from this multi-sensor methodology is anticipated to be used by researchers, lake resource managers, and citizens to expedite the pre-processing steps so that actionable information can be retrieved for decision making.

1. Introduction

The abundant surface waters in Minnesota face multiple threats from land-use change, eutrophication, invasive species, and warming temperatures (Bossenbroek et al., 2001; O'Reilly, 2015; Smith, 2016). Protecting water quality is critically important to lake-rich states because of the ecological and economic importance of water activities and tourism. To understand and ensure the sustainability of these aquatic ecosystems on a statewide scale, adoption of publicly available satellite Earth observation data will be necessary for effective management. While traditional *in situ* sampling methodologies can provide rapid, accurate information about targeted lakes, sampling more than a fraction of > 10,000 is laboriously challenging. On the other hand, research efforts using Landsat data to model water quality parameters such as turbidity and algal pigment concentration across inland lakes date as far back as 1978 (Carpenter and Carpenter, 1983). Two of the most relevant for Minnesota lakes is the water clarity image processing protocol developed by Olmanson et al. (2001) and Kloiber et al. (2002a) using Landsat Thematic Mapper (TM) and Multi-spectral Scanner (MSS) sensor data. Since then, the launch of Landsat-8 (13-Feb 2013) carrying the Operational Land Imager (OLI) and the European Space Agency's (ESA) Sentinel-2A (23-Jun 2015) and 2B (7-Mar 2017) MultiSpectral Imager (MSI) constellation have advanced the capabilities of water quality products that can be derived from remote sensing systems (Tyler et al., 2016; Pahlevan et al., 2017a; Pahlevan et al., 2017b).

While interest has increased since earlier studies (Kloiber et al., 2002a, 2002b), routine monitoring of lake water quality using satellite remote sensing is still not a common practice by resource management agencies; particularly, at a time when moderate resolution imagery is

* Corresponding author.
E-mail address: pagex135@umn.edu (B.P. Page).

https://doi.org/10.1016/j.rse.2019.111284
Received 4 September 2018; Received in revised form 24 June 2019; Accepted 25 June 2019

readily available from repository platforms like ESA's Copernicus Open Access Hub, Amazon Web Services, and the U.S. Geological Survey (USGS) Earth-Explorer at no cost. The absence of satellite remote sensing strategies for routine monitoring of lake water quality parameters on a statewide basis likely is attributable to the computational demands required for managing and analyzing the large volume of statewide imagery using common processing software. To this end, high performance and cloud-computing infrastructures will aid in image processing experimentation and efficiency. For example, Google's Earth Engine (GEE) cloud computational platform houses petabytes of imagery and other auxiliary geospatial datasets that can be accessed through a JavaScript application programming interface (Gorelick et al., 2017), and dense temporal MSI and OLI datasets can be seamlessly searched, handled and processed at a significantly faster rate.

The overall objectives of this research were to (1) implement modified atmospheric correction formulas into the GEE platform to produce harmonized remote sensing reflectance (R_{rs}) products between MSI and OLI imagery, and (2) demonstrate the applicability of the validated R_{rs} products by mapping water clarity (SD) across Minnesota's optically variable and temporarily dynamic inland lakes. Recently, the capability of both MSI and OLI to yield similar reflectance values has been shown to be feasible for both water (Vanhellemont and Ruddick, 2016; Page et al., 2018; Pahlevan et al., 2019) and land (Claverie et al., 2018), and investigating further into these capabilities in the GEE platform allow for faster cross-sensor experimentation than using conventional image processing techniques. In terms of water clarity model development, the Secchi depth (SD) relies heavily on multispectral channels centered in the blue to red region (typically 443 nm to 670 nm) of the electromagnetic spectrum (Harrington and Schiebe, 1992; Giardino et al., 2001; Olmanson et al., 2013; Lee et al., 2016), where the combination of ozone (absorbing) and Rayleigh (scattering) effects may constitute as much as 90% of the total top-of-atmosphere reflectance (ρTOA) received by the satellite sensor (Gordon et al., 1997; Mishra et al., 2005). If we are to take advantage of available imagery for near real-time monitoring at higher frequencies, a consistent correction to compensate for the temporal variations in atmospheric properties in these wavelengths is necessary, and anticipated to strengthen future and existing models of water clarity. However, the consistency of any atmospheric correction over time across optically variable inland lakes is not yet fully understood. To address this matter, we processed MSI and OLI imagery using our Modified Atmospheric correction for INland waters (MAIN) (described in Section 2.3) within the GEE environment and compared the generated R_{rs} values against the R_{rs} values converted from the USGS L8 Surface Reflectance Product (OLI-SR) as a reference. Further, an external image processing software (ACOLITE, Vanhellemont and Ruddick, 2015, version 20,190,326) also equipped to generate R_{rs} products from MSI and OLI imagery was included in the comparison to provide a secondary means of performance.

If the long-term goal is to develop reliable and cost-effective approaches to regional measurements of major indicators of water quality that can be used by management agencies to extend ground-based measurements (Olmanson et al., 2008; Olmanson et al., 2001; Kloiber et al., 2002b) then development of automated approaches that can take advantage of the improved spectral, spatial, radiometric and temporal resolution of the MSI and OLI systems are needed for improved water quality monitoring and fisheries management. Here, a SD model is developed from atmospherically corrected MSI imagery using a robust *in situ* SD dataset ($SD_{in\ situ}$) collected from the Citizen Lake Monitoring Program (CLMP), coordinated by the Minnesota Pollution Control Agency (MPCA, www.pca.state.mn.us/water/resources-volunteers) across three ecoregions in Minnesota, USA. Significant band-ratios in predicting SD were chosen based on a bootstrap forest technique (Breiman, 1996). Considering the spectral and spatial similarities between five MSI and OLI sensor bands in the visible and NIR portion of the electromagnetic spectrum (Table 1), a more restricted SD model was developed for MSI using comparable OLI bands (SD_{sOLI}) so that the model may be extrapolated to OLI data to increase overall temporal resolution when using both sensors for multi-platform water clarity assessments. The data derived from this consistent multi-sensor methodology are anticipated to be used by lake resource managers and agencies, researchers and citizens to eliminate the pre-processing steps for satellite imaging applications so that actionable information can be readily retrieved for decision-making.

2. Methodology

2.1. Study area

The study area was intended to target as many of the > 12,000 inland surface waters across the state of Minnesota, USA as possible using Level-1 MSI and OLI imagery provided in the GEE repository. Positioned in the upper Midwest United States at 43.4–49.4° N, 89.4–96.8° W, Minnesota's vast collection of optically variable water bodies is spread across seven ecoregions (Fig. 1), geographical areas where the land cover (agriculture, forest, prairie, *etc.*), underlying geology, soils, and potential native plant community are relatively similar (Omernik, 1987). Four of these ecoregions include ~96% of Minnesota's lakes. The Northern Lakes and Forest Ecoregion (NLF), with 46% of the state's lakes, has a higher concentration of optically clearer waters (lower chlorophyll) and lakes with higher colored dissolved organic matter (CDOM) (Brezonik et al., 2019). The North Central Hardwood Forests Ecoregion (NCHF), with roughly 38% of the state's lakes, has a wide range of water clarity. Lakes in the Western Corn Belt Plains Ecoregion (WCBP), which has 7% of the state's lakes, generally are more eutrophic and have low water clarity. The Northern Glaciated Plains (NGP) Ecoregion, with 6% of the lakes, also has low water clarity. Statewide assessments for > 10,500 lakes using Landsat data revealed that water clarity has remained stable between 1985 and 2005 in the NLF and NCHF ecoregions but declined slightly in the WCBP and the NGP (Olmanson et al., 2013).

2.2. Satellite data and image pre-processing

Different data sets of S2A/MSI and L8/OLI imagery were searched from the GEE repository and allocated for either atmospheric correction assessment and/or SD model calibration/validation (Table 2). For SD model calibration and validation we targeted mostly clear imagery acquired from a late-summer index period (July 15–September 15) when short-term variability and water clarity are at a seasonal minimum (Stadelmann et al., 2001). Before any statistical evaluation or performance assessment, all L8/OLI Level-1 imagery were first converted from the digital number (DN) format into TOA reflectance (ρTOA):

$$\rho TOA,_{\,\mathrm{OLI}} = M_{L}(\lambda_i) \times DN_{\mathrm{OLI}}(\lambda_i) + A_{L}(\lambda_i) \tag{1}$$

where ρTOA is the top-of-atmosphere spectral reflectance measured by the OLI sensor at wavelength λ_i, and M_L and A_L are the band multiplicative and additive coefficients found in the image metadata (Landsat-8 Data Users Handbook, V2.0). For S2/MSI, Level-1C ρTOA is achieved by multiplying the imagery by the scaling factor (0.0001).

Next, surface water bodies were isolated by masking out surrounding terrestrial features using a threshold technique in the SWIR portion of the spectrum. A simple threshold value (0.03) was assigned to a mosaicked image which consisted of a statewide median value from the SWIR band (B7 at 2201 nm) from the entire collection of Tier-1 L8 Surface Reflectance Product (OLI-SR) with < 2% cloud cover over Minnesota between 2013 and 2018 (n = 172). Imagery between June and October were used for masking to avoid snow and lake-ice contaminated pixels. A masking threshold of 0.03 worked well to separate the high absorbing water features from the surrounding landscape in this area, but this value may need some adjustment for other geographical regions. Once the pre-processing steps were finalized, we

Table 1
Sensor characteristics for L8/OLI and S2/MSI, including bandcenter, bandwidth, spatial resolution and signal-to-noise ratio (SNR). SNR values have been scaled for radiances observed over clear coastal waters.
(Adopted from Pahlevan et al., 2017b.)

Landsat-8/OLI

Band ID	B1	B2	B3	B4	–	–	–	–	B5	B6	B7
Band center (nm)	443	482	561	655	–	–	–	–	865	1609	2201
Bandwidth (nm)	20	65	60	40	–	–	–	–	30	85	190
Resolution (m)	30	30	30	30	–	–	–	–	30	30	30
Signal-to-Noise Ratio (SNR)	284	321	223	113	–	–	–	–	45	10.1	7.4

Sentinel-2/MSI

Band ID	B1	B2	B3	B4	B5	B6	B7	B8	B8A	B11	B12
Band center (nm)	444	497	560	664	705	740	783	842	865	1610	2190
Bandwidth (nm)	20	55	35	30	15	15	15	15	20	9	175
Resolution (m)	60	10	10	10	20	20	20	10	20	20	20
Signal-to-Noise Ratio (SNR)	439	102	79	45	45	34	26	20	16	2.8	2.2

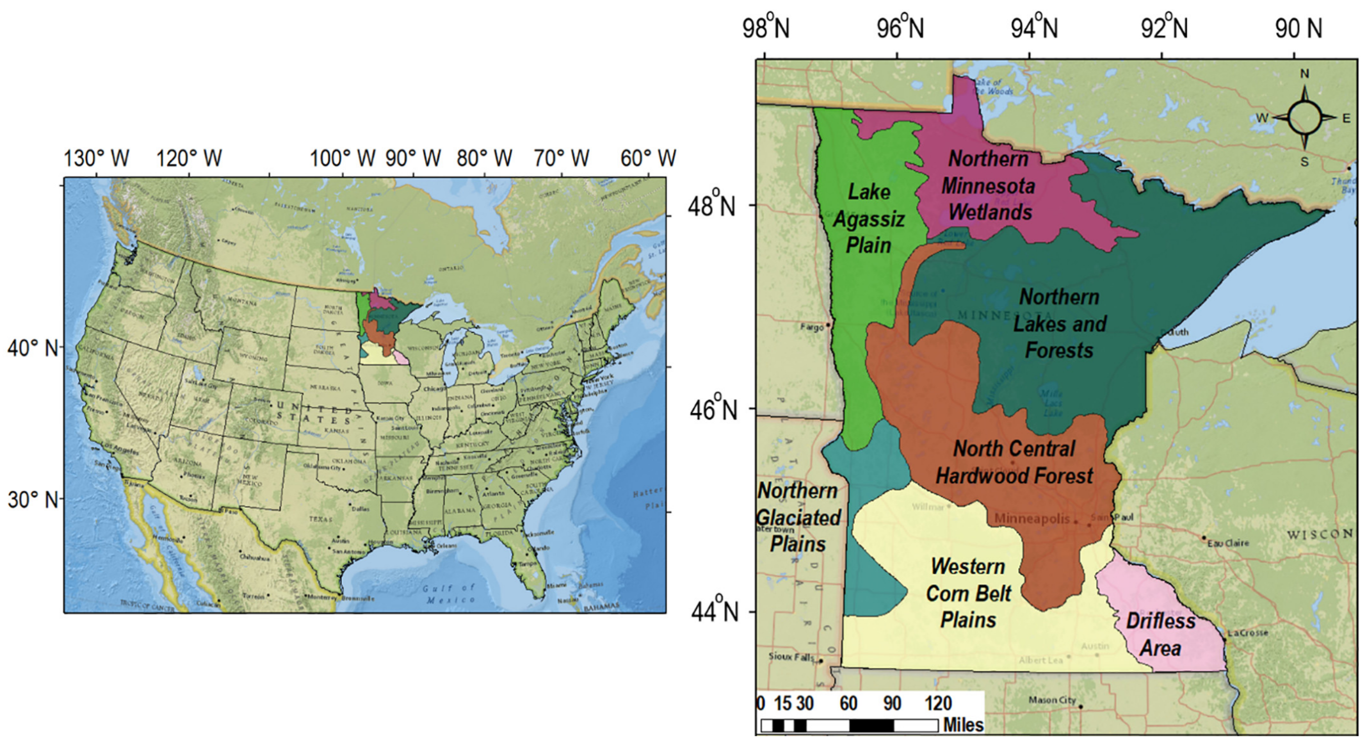

Fig. 1. Study area. Minnesota, USA and its corresponding ecoregions. Basemap source: National Geographic, Esri, Garmin, HERE, UNEP-WCMC, USGS, NASA, ESA, METI, NRCAN, GEBCO, NOAA, INCREMENT P.

Table 2
Image dates and ID(s) of S2/MSI and L8/OLI scenes used in the study along with the allocated application.

Date	GEE Scene ID	Application	n
23-Aug-17	COPERNICUS/S2/20170823T170849_20170823T171828_T15	SD model calibration	79
12-Sep-17	COPERNICUS/S2/20170912T170949_20170912T171451_T15	SD model validation	276
27-Sep-17	COPERNICUS/S2/20170927T172111_20170927T172106_T15TVK LANDSAT/LC08/C01/T1/LC08_027029_20170927	Atmospheric correction assessment, SD model validation	18
13-Aug-18	COPERNICUS/S2/20180813T170851_20180813T172023_T15TVK LANDSAT/LC08/C01/T1/LC08_027029_20180813	SD model validation	43

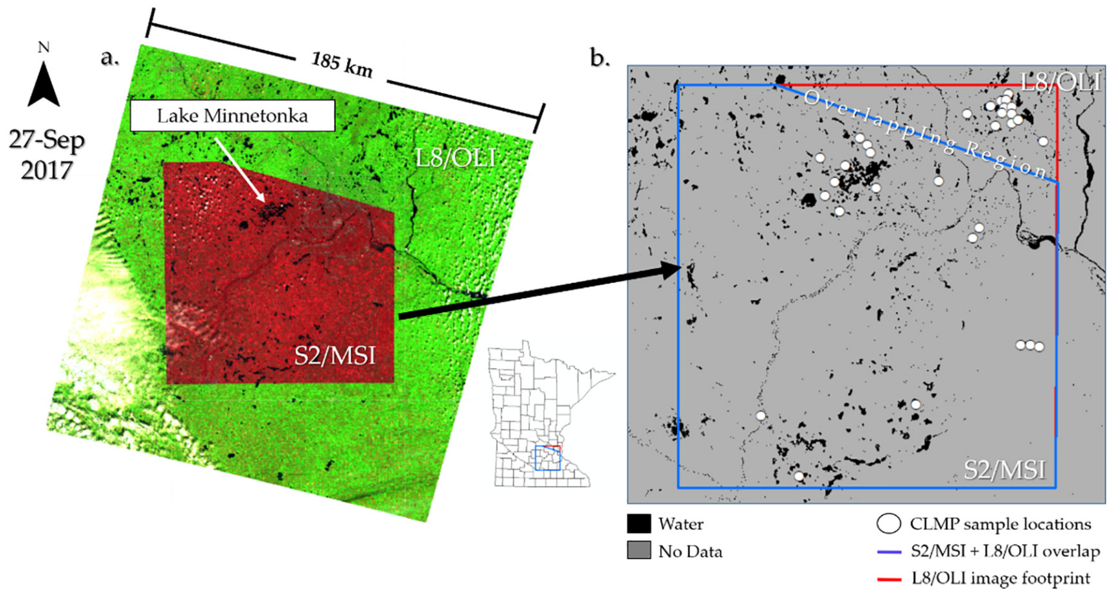

Fig. 2. False color composites of the coincident overpass imagery between L8-L1T Path 27, Row 29 (ID: LANDSAT/LC08/T1/LC08_027029_20170927) at 11:59 am CST (RGB: B7/B5/B2) and S2-L1C (ID: COPERNICUS/S2/20170927T172111) sub-track of T15TVK at 12:21 pm CST on 27-Sep 2017 (RGB: B8A/B4/B3) (a). Sampled locations by CLMP (white circles) outside the overlapping region between MSI and OLI (blue line) were excluded (b). (For interpretation of the references to color in this figure legend, the reader is referred to the web version of this article.)

applied atmospheric correction (Section 2.3) to the collection of targeted MSI and OLI imagery for further analysis (Section 2.4).

2.3. Modified atmospheric correction for INland waters (MAIN)

We adopted atmospheric correction theory from traditional ocean-color techniques (Hu et al., 2000; Wang et al., 2009; Werdell et al., 2010; Dash et al., 2012; Vanhellemont and Ruddick, 2015), where the desired water-leaving reflectance (ρ_w) and subsequent remote-sensing reflectance (R_{rs}) (an apparent optical property) is derived (Gordon et al., 1983):

$$\rho_w(\lambda_i) = \rho_{rc}(\lambda_i) - \rho_{am}(\lambda_i)/t(\lambda_i) \tag{2}$$

$$R_{rs}(\lambda_i) = \rho_w/\pi \tag{3}$$

where $t(\lambda_i)$ is the diffuse transmittance from the water surface to the satellite (Hu et al., 2004). ρ_{rc} is the Rayleigh corrected reflectance (Gordon and Wang, 1994; Dash et al., 2012) and includes other correction factors including the Rayleigh scattering phase function (Doerffer, 1992) Fresnel correction (Gordon and Wang, 1994) as well as the ozone adjustment (Mishra et al., 2005; Dash et al., 2012). The ozone absorption coefficient for each spectral band was taken from the Aerosol Optical Depth Value-Added Product (Koontz et al., 2013) and the daily measured ozone concentration obtained from the merged products of Total Ozone Mapping Spectrometer (TOMS) Earth Probe, TOMS/Nimbus-7, TOMS/Meteor-3, and the Ozone Monitoring Instrument (OMI) available in the GEE repository (collection ID: TOMS/MERGED). Additionally, a digital elevation model (DEM) from the Shuttle Radar Topography Missions (SRTM, 30 m) (Farr et al., 2007) was used to calculate the Rayleigh optical thickness (Hansen and Travis, 1974) on a pixel-by-pixel basis.

The strong impact of the aerosol path reflectance (ρ_a) in the visible and NIR spectral range can be difficult to correct as complex scattering and absorbing properties of aerosols vary spectrally and with aerosol size, shape, chemistry and density (Vermote et al., 2016). Previous research has demonstrated that observations of optically turbid water pixels within the Rayleigh- corrected shortwave infrared (SWIR) channels have comparable signal responses to that of clear water pixels (Wang et al., 2009; Werdell et al., 2010; Vanhellemont and Ruddick, 2015). Aerosol path radiance reflectance has been expressed as (Gordon and Wang, 1974):

$$\rho_a(\lambda_{NIR}) = ke^{(-c\,\lambda)} \tag{4}$$

where k and c are constants. Assuming negligible signal in the SWIR wavelengths even in the most optically complex waters (Vanhellemont and Ruddick, 2015), the two Rayleigh-corrected SWIR bands available on the MSI and OLI ($\rho_{rc}(\lambda_{SWIR\text{-}1,2})$) were used for aerosol determination rather than the NIR band, where the optically active constituents (OACs) in meso- to hyper-eutrophic inland lakes usually interfere with the NIR signal:

$$\rho_{rc}(\lambda_{SWIR-1}) = ke^{(-c\,\lambda)} = \rho_{rc}(\lambda_{SWIR-2}) \tag{5}$$

Aerosol type ε was then determined for each pixel as the negative of the slope of the straight line (Hu et al., 2000; Dash et al., 2012) between $\Delta\lambda_{SWIR\text{-}1,2}$ and $\Delta Ln(\rho_{rc}(\lambda_{SWIR\text{-}1,2}))$ as:

$$(Ln(p_{rc}(\lambda_{SWIR-2})) - Ln(p_{rc}(\lambda_{SWIR-1}))/(\lambda_{SWIR-2} - \lambda_{SWIR-1}) = -\varepsilon \tag{6}$$

The output returns a raster image of ε which was extrapolated to the visible and NIR bands:

$$\rho_{am}(\lambda_{VIS-NIR}) = \rho_{rc}(\lambda_{SWIR-2}) \times (F_0'/F_0'(\lambda_{SWIR-2}))e^{(-\varepsilon\times(\lambda i/\lambda swir-2))} \tag{7}$$

where F_0' is the instantaneous extraterrestrial solar irradiance adjusted for Earth-sun distance (Dash et al., 2012) and ρ_{am} is the aerosol reflectance map needed to quantify the remaining contributions from aerosols across each spectral band. Although the MSI and OLI sensors were not developed specifically for inland aquatic applications, the provided variables within the image metadata allow to fulfill the necessary equations to derive R_{rs} in the GEE environment.

2.4. Evaluation of MSI and OLI R_{rs} products

First, we assessed MAIN derived R_{rs} values using imagery acquired during a coincident overpass between MSI and OLI on 27-Sep 2017 (Table 2) over a region with a wide range of water clarity, the Lake Minnetonka area in east-central Minnesota (Fig. 2a). Within the overlapping region of the MSI and OLI footprint, Corresponding SD measurements from 18 optically variable inland lakes were sampled by participants at the Citizen Lake Monitoring Program (CLMP)

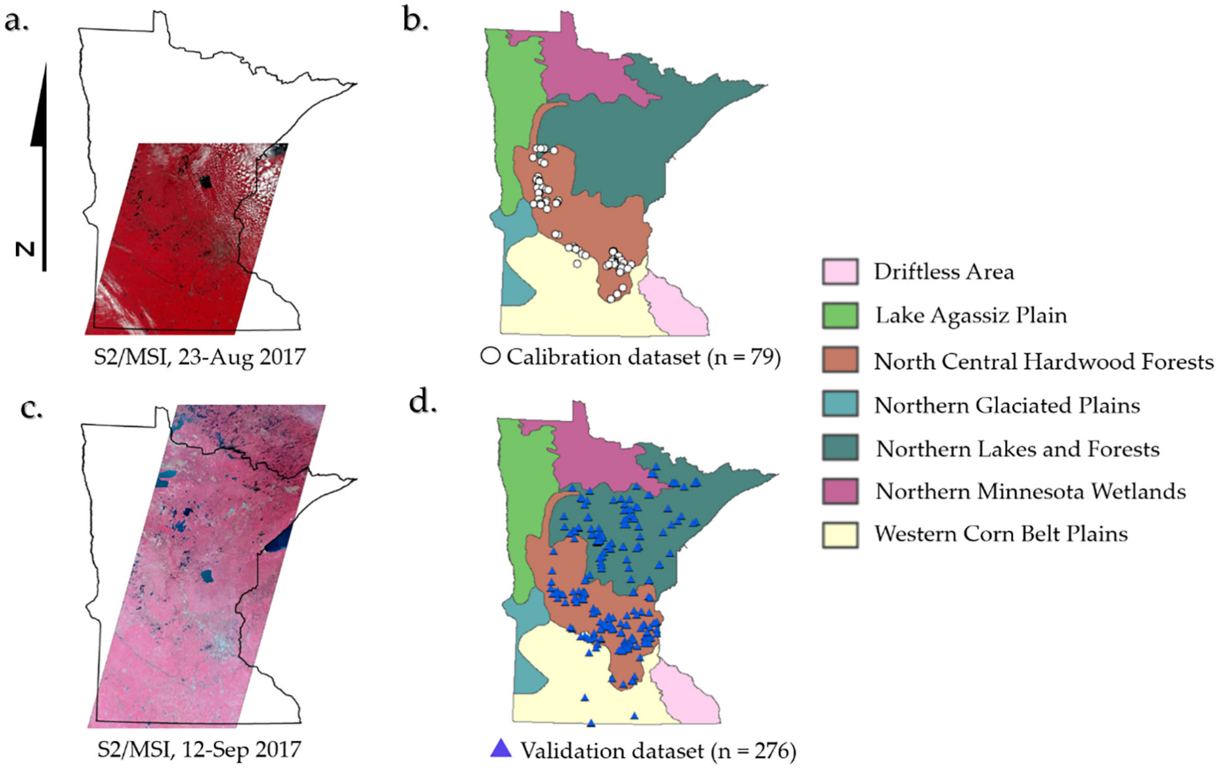

Fig. 3. False color MSI image composite (RGB: B8A/B4/B3) over Minnesota on 23-Aug 2017 (a) and on 12-Sep 2017 (c). Time-window qualified $SD_{in\ situ}$ sample locations collected by CLMP (± 1 day within satellite overpass) across the WCBP, NCHF, and NLF ecoregions are represented as white circles for the SD model calibration (b) and blue triangles for model validation dataset (d). (For interpretation of the references to color in this figure legend, the reader is referred to the web version of this article.)

within ± 1 day of the coincident overpass event (Fig. 2b). Any samples that fell beyond the overlapping footprints were excluded, because MSI imagery during 2017 was limited over the USA and for that date only covered a portion of southern Minnesota. Sampled point location data were uploaded to a GIS and transformed to a 50 m circular buffer around the centroid. Corresponding mean satellite ρTOA and R_{rs} values of pixel regions within the polygons were then extracted and tabulated. Prior to pixel extraction, MSI pixels were resampled to 30 m and registered to match the OLI georeferenced image prior to comparison (Storey et al., 2016).

In the absence of radiometric reference measurements such as buoy or other suitable matchup data for the Minnesota water bodies, several researchers have demonstrated that the inter-comparison of other atmospheric corrections represents an alternative option (Suresh et al., 2006; Vanhellemont and Ruddick, 2014; Bernardo et al., 2017). To this end, we evaluated MAIN derived MSI and OLI R_{rs} image products by evaluating the statistical closeness with R_{rs} values converted from the USGS Landsat-8 Surface Reflectance Product (OLI-SR), readily available in the GEE repository. Previous evaluations of MSI and OLI derived R_{rs} products have included the ocean color component of the Aerosol Robotic Network (AERONET-OC), inter-comparisons and cross-calibrations against other ocean color products, and optimizations of vicarious calibration gains (Pahlevan et al., 2017a, Pahlevan et al., 2017b, Ilori et al., 2019). In this study, lacking AERONET sites, OLI-SR spectra were defined as the closest representation of reference spectra considering previous successful reports on using OLI-SR with corresponding *in situ* water quality data for inland aquatic applications (Kuhn et al., 2019; Slonecker et al., 2016; Bernardo et al., 2017; Markert et al., 2018). We evaluated MAIN and ACOLITE derived R_{rs} values by calculating the root mean square difference (RMSD) across each multispectral band (λ_i) against the OLI-SR product:

$$\mathrm{RMSD}(\lambda i) = \frac{\sqrt{\sum_{i=1}^{n}(x_{Rrs}(\lambda i) - x_{SR}(\lambda i))^2}}{n}(\mathrm{unit{:}sr} - 1) \tag{8}$$

where x_{Rrs} are the mean R_{rs} values from the sampled pixel regions using either the MAIN or ACOLITE method and x_{SR} is the OLI-SR reference spectra. Further, the same OLI and MSI coinciding overpass imagery were processed outside of GEE using ACOLITE (Vanhellemont and Ruddick, 2015) as a secondary comparison to provide a relative base on how well MAIN derived MSI and OLI R_{rs} values were performing over aquatic surfaces.

Next, we assessed the relative signal responses across comparable wavelengths (Table 1) using same MSI and OLI coincident imagery before and after atmospheric correction through mean absolute percent difference (MAPD%) in addition to the coefficient of determination (R^2) to evaluate cross-sensor consistency:

$$\mathrm{MAPD}(\lambda i) = \frac{\sum |x_{\mathrm{OLI}(\lambda i)} - x_{MSI(\lambda i)}|}{x_{OLI(\lambda i)}} \times 100 \tag{9}$$

where x_{MSI} and x_{OLI} are either the mean ρTOA or R_{rs} values for MSI and OLI at wavelength *i*, respectively.

2.5. Water clarity model calibration

SD is the most commonly measured water quality variable and has been shown to be strongly correlated with Landsat blue and red spectral bands (Kloiber et al., 2002a, 2002b; Olmanson et al., 2008). Corresponding blue and red (B2 and B4, respectively) MSI bands were hypothesized to contribute the most significance for SD model calibration purposes. Previous empirical methodologies for developing water clarity models involved direct stepwise linear regression between log-transformed $SD_{in\ situ}$ ($\ln SD_{in\ situ}$) and Landsat derived reflectances (Olmanson et al., 2001; Olmanson et al., 2013; Kloiber et al., 2002a, 2002b; Lillesand et al., 1983). However, the MSI sensor has three additional red-edge bands (Table 1), one of which (B5, centered at ~705 nm) has been demonstrated to improve chlorophyll measurements (Gitelson et al., 2007; Gitelson et al., 2009; Mishra et al., 2013; Olmanson et al., 2015) thus providing the potential of yielding more reliable water clarity estimates. To explore the potential of these bands in predicting water clarity, we implemented a bootstrap forest technique within the JMP Pro 14 software (JMP®, Version 14. SAS Institute Inc., Cary, NC, 1989–2007) that informs the most significant bands and band-ratio combinations to model $\ln SD_{in\ situ}$.

The calibration dataset consisted of 79 $\ln SD_{in\ situ}$ measurements obtained by the Citizen Lake Monitoring Program (CLMP) collected within ± 1 day of the clear portions of the 23-Aug 2017 imagery (Fig. 3a-b) as the dependent variable and MAIN derived mean MSI-R_{rs} values from bands B1-B8A (443–865 nm) and all band ratio permutations as independent input parameters (47 total terms). The bootstrap forest technique uses many decision trees to associate input terms with calibration/validation data, chosen in part randomly to determine the most significant terms that predict a response variable ($\ln SD_{in\ situ}$) based on the highest total sum of squares (SSTO) (Hastie et al., 2009). Prediction consistency of the bootstrap decision for each term was evaluated by splitting the samples into training (70%) and validation (30%) datasets and run for 10,000 iterations. Here, only two of the most contributing terms that produced highest coefficient of determination (R^2) with 79 $\ln SD_{in\ situ}$ measurements collected across the WCBP, NCHF, and NLF ecoregions of Minnesota were used for SD model development. We restricted to two-terms only so that they are consistent with water clarity models developed in the past (Kloiber 2002a, 2002b: Olmanson et al., 2008). Further, a second model was developed for MSI except the three red-edge (B5-B7) bands and one NIR band (B8) which are absent on the OLI sensor were excluded for consideration in order to establish a robust water clarity model for both platforms (SD_{sOLI}). Overall model accuracy was then assessed on how well the calibrated SD_{MSI} (and SD_{sOLI}) model forecasted $SD_{in\ situ}$ and was evaluated using the mean absolute error (MAE) as they are less sensitive to outliers (Seegers et al., 2018):

$$\mathrm{MAE} = \frac{\sum_{i=1}^{n} |SD_{sensor} - SD_{in\,situ}|}{n} \tag{10}$$

where SD_{sensor} is either SD_{MSI} or SD_{sOLI}, and a value of 0 is desired.

2.6. Water clarity model validation

For SD model validation, we first applied our calibrated SD_{MSI} model on an S2A/MSI image acquired on 12-Sep 2017 (Table 2) against 276 corresponding SD measurements collected by the CLMP ± 1 day of satellite overpass (Fig. 3c-d). Accuracy of all SD models were determined through MAE with corresponding $SD_{in\ situ}$ data. To evaluate the consistency of the SD_{MSI} and SD_{OLI} models on a more temporal scale, two coinciding overpass images at different dates were used as secondary and tertiary SD model validation datasets. In addition to the 18 $SD_{in\ situ}$ measurements corresponding with the coincident MSI/OLI overpass imagery acquired on 27-Sep 2017 used to evaluate atmospheric correction (Fig. 2b), a second image pair acquired on 13-Aug 2018 over the same region (not displayed) was also included in the validation process and introduced another unique 43 $SD_{in\ situ}$ measurements (Table 2). It is important to note that the ranges of the secondary and tertiary 18 and 43 $SD_{in\ situ}$ measurements collected on 27-Sep 2017 (2^0) and 13-Aug 2018 (3^0) are 0.30–7.00 m and 0.45–6.70 m, respectively. These are comparable ranges used in the MAIN-derived SD_{MSI} (and SD_{sOLI}) calibration (0.20–6.70 m) on 23-Aug 2017 and 1^0 validation (0.43–6.7 m) dataset on 12-Sep 2017 (Fig. 4), thus capturing the representational range of water clarity seen in Minnesota on a statewide scale in a single tile.

3. Results and discussion

3.1. Atmospheric correction

With the absence of *in situ* radiometric data in the Minnesota region for spectral comparison with MAIN derived MSI-R_{rs} and OLI-R_{rs} values, R_{rs} values converted from the USGS OLI-SR product (R_{rs} = OLI-SR / π) were used as reference (Section 2.4). Overall, both MAIN and ACOLITE methods yielded R_{rs} values comparable to the USGS OLI-SR product for both MSI and OLI from the 18 lakes sampled for atmospheric correction (Fig. 5).

The higher RMSD in the MSI-R_{rs} spectra relative to OLI-R_{rs} was expected due to the differences in the signal-to-noise ratio (SNR) (Table 1) of the MSI sensor rather than the direct OLI to OLI-SR comparison. Interestingly, R_{rs} values in the blue, green and red bands (B2-B4) resulting from both MAIN and ACOLITE yielded the lowest RMSD across comparable bands relative the reference spectra. This is important as these bands have been shown to contribute the highest significance in estimating SD for sensors used in previous research (Olmanson et al., 2013; Olmanson et al., 2001; Kloiber, 2002), and were considered as target variables for developing water clarity models (Section 2.5). Regardless of the higher RMSD, the mean R_{rs} spectra derived from ACOLITE share similar shape and magnitude relative to both MAIN and OLI-SR datasets from the 18 sampled lakes (Fig. 6). This provided confidence in the MAIN R_{rs} products considering the reasonable matchup with ACOLITE over aquatic surfaces and especially the OLI-SR product which was not originally intended for aquatic applications.

We also analyzed the relative signal response between MAIN and ACOLITE derived MSI and OLI reflectance values before and after atmospheric correction to evaluate cross-sensor performance. First, MSI-R_{rs} and OLI-R_{rs} values produced from MAIN outlined in Section 2.3 most notably generated positive (non-negative) values across all comparable spectral bands (Fig. 7), where negatives values have been commonly observed in previous studies due to inconsistent atmospheric correction in optically variable regions, resulting in masked pixels values with no data (Werdell et al., 2010; Bailey et al., 2010; Dash et al., 2012).

The mean absolute percent difference (MAPD%) in ρTOA values between MSI and OLI prior to correction were all < 10% in the visible bands but ~14% in the NIR band (Fig. 8). ρTOA R^2 values were slightly lower between the MSI and OLI coastal band (R^2 = 0.61) and even less in the NIR band (R^2 = 0.36), however, the signal response between MSI and OLI ρTOA blue, green and red bands exhibit nearly synchronized readings, with R^2 = 0.92, 0.98, and 0.96 respectively (Fig. 9a). Correlation differences observed in the coastal band were likely due to downscaling from the native 60 m spatial resolution to match OLI at 30 m (Mandanici and Bitelli, 2016), while the NIR band could again be attributed to the SNR difference between the two sensors or other inherent signal characteristics (Pahlevan et al., 2017b) (Table 1). After atmospheric corrections, band-by-band PD between MSI and OLI R_{rs} values mostly remained low as seen in the ρTOA comparison (Fig. 8). After MAIN processing, band-by-band R^2 values were conserved (Fig. 9b), and a similar 1:1 signal response in the band-by-band comparison after ACOLITE processing (Fig. 9c) suggested the suitability of using MAIN for aquatic applications. Harmonized R_{rs} products between the MSI and OLI were seen again after MAIN processing using another coincident overpass date acquired on 13-Aug 2018 (Fig. 10), again showing highest MAPD% in the coastal (B1) and NIR (B5) bands. These results show that the conservation in the R^2 values of the relative signal response between MSI and OLI and the consistently low relative MAPD after MAIN processing allow for relatively consistent R_{rs} retrievals from both sensors on a temporal scale regardless of atmospheric effects. More importantly, it allows for the development of consistent water clarity (and other water quality) models across both MSI and OLI sensors so that both datasets can be incorporated in time series analysis. From here, efforts can be made by lake management practices to improve the

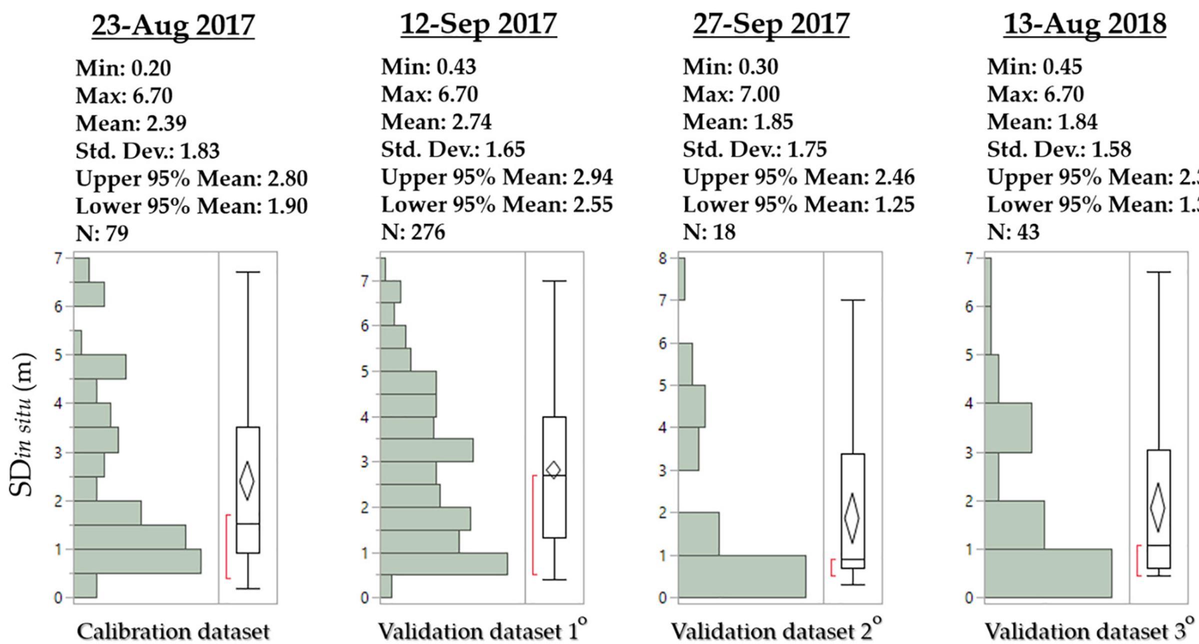

Fig. 4. Comparable statistics and corresponding histogram plots of *in situ* water clarity ($SD_{in\ situ}$) distribution from the calibration and three validation datasets.

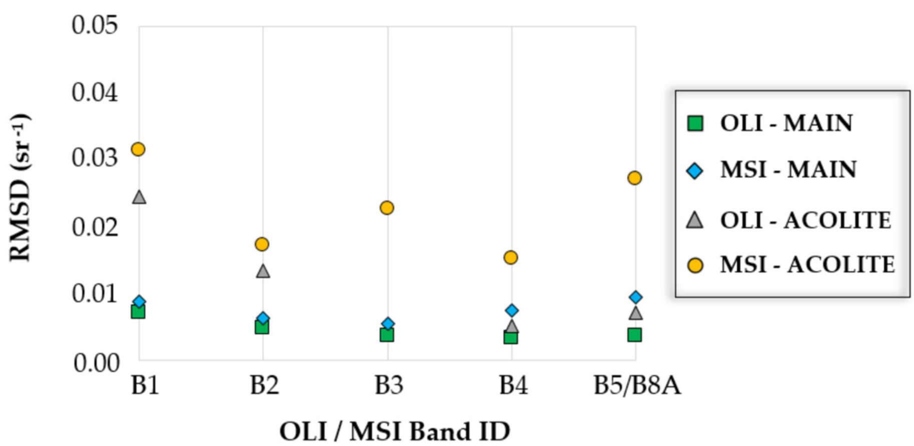

Fig. 5. Comparable RMSD (unit: sr^{-1}) values between MAIN and ACOLITE corrected MSI and OLI R_{rs} bands against the USGS OLI-SR reference spectra during a MSI/OLI coinciding overpass on 27-Sep 2017 (n = 18).

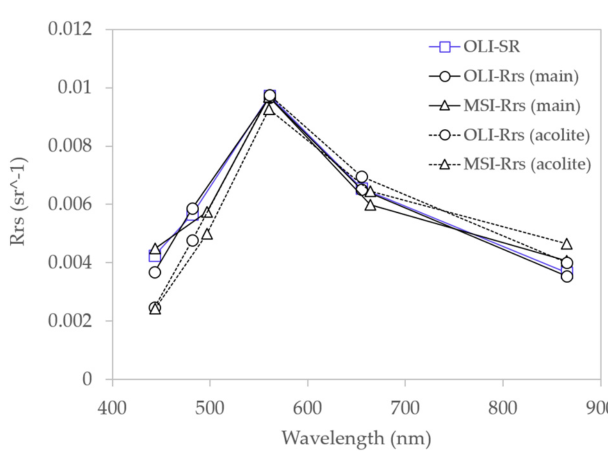

Fig. 6. Comparable MSI and OLI spectra derived from MAIN (solid line) and ACOLITE (dashed line) against the OLI-SR product (blue line) using the mean R_{rs} values from the 18 locations from the 27-Sep 2017 coincident overpass imagery. (For interpretation of the references to color in this figure legend, the reader is referred to the web version of this article.)

overall accuracy of the derived R_{rs} products for select study sites for continuous monitoring purposes. The overall accuracy of the generated MSI-R_{rs} and OLI-R_{rs} values would improve with frequent, routine *in situ* radiometric and water quality parameter measurements in a more systematic manner to fully understand the relationships between R_{rs} and the OACs for a particular optically variable water body.

3.2. Water clarity model calibration

Our next objective was to evaluate the applicability of the generated MSI and OLI R_{rs} products from MAIN in mapping water clarity (in terms of SD) (Section 2.5). Previous research on mapping water clarity in Minnesota used mainly a consistent blue/red, and blue 2-term model (Kloiber et al., 2002a, 2002b) calibrated through multiple linear regression analysis using Landsat satellite spectral data and corresponding $SD_{in\ situ}$ measurements (Olmanson et al., 2008; Olmanson et al., 2016). Here, we used a bootstrap forest method to obtain model-independent indicators of the most important predictors of water clarity using the 23-Aug 2017 calibration dataset (Section 2.5). The bootstrap forest technique was necessary in this case as the additional spectral bands of MSI (relative to OLI) could improve water clarity estimates. Of

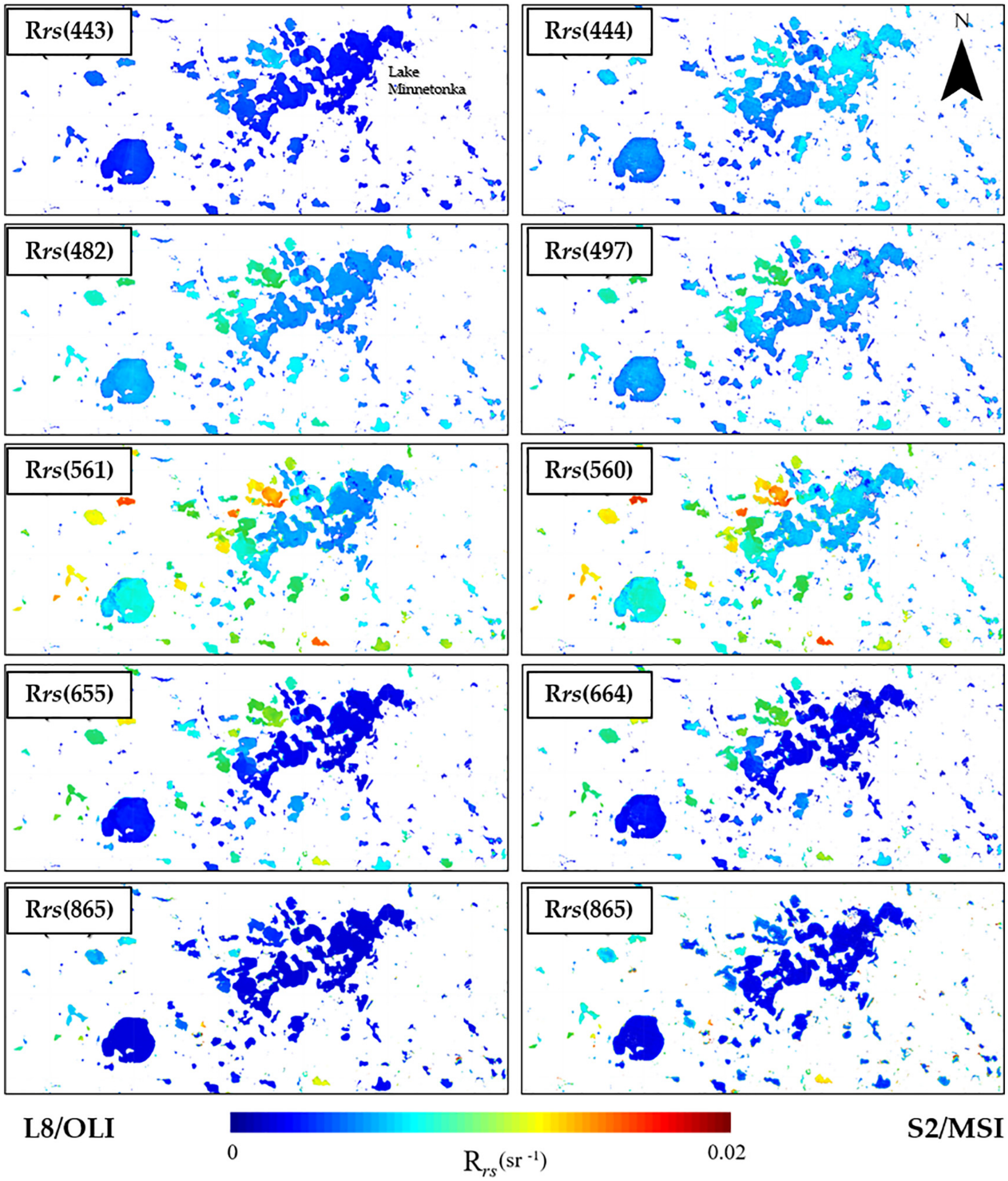

Fig. 7. Pseudocolor maps of comparable OLI-R_{rs} (left) and MSI-R_{rs} (right) products over Lake Minnetonka, MN and surrounding water bodies during the coinciding overpass on 27-Sep 2017.

the 47 terms tested as input predictors for $\ln SD_{in\ situ}$, the two terms yielding the highest sum of squares (SSTO) from the bootstrap forest were MSI-R_{rs}(B2/B4) and MSI-R_{rs}(B5 × B4). The MSI-R_{rs}(B2/B4) ratio was expected to be a contributing candidate in predicting $\ln SD_{in\ situ}$ as previous successes using prior Landsat satellites have been documented (Olmanson et al., 2008; Olmanson et al., 2016). These two terms resulting from the bootstrap forest generated the most favorable linear regression ($R^2 = 0.88$) with $\ln SD_{in\ situ}$ and took the form:

$$\ln SD_{MSI} = a_{MSI}\,(R_{rs}(B2)/R_{rs}(B4)) + b_{MSI}\,(R_{rs}(B5) \times R_{rs}(B4)) + c_{MSI} \tag{11}$$

where coefficients a_{MSI} (2.4367945), b_{MSI} (−2717.821), and c_{MSI} (−2.468818) were fit to the calibration data and $\ln SD_{MSI}$ is the log-transformation of the desired MSI derived SD (SD_{MSI}) for a given pixel (Fig. 11a). From these results it is clear that the MSI-R_{rs}(B5) is a major contributor to water clarity prediction, a considerable advantage over the OLI sensor. The capability of the MSI-R_{rs}(B5) band to be used as a predictor for water clarity makes sense as chlorophyll-a exhibits strong reflectance in the 705–708 nm spectral region, and is often used in satellite-derived algal indices (Mishra et al., 2013; Augusto-Silva et al., 2014; Watanabe et al., 2015; Ogashawara et al., 2017).

An additional lnSD model was developed using the 23-Aug 2017 MSI imagery where only the comparable OLI bands were used as the independent variables ($\ln SD_{sOLI}$). Here, the MSI-R_{rs}(B2)/R_{rs}(B4) ratio again resulted as the highest contributing candidate (in terms of SSTO) for predicting $\ln SD_{in\ situ}$, followed by the green band (B3). The $\ln SD_{sOLI}$ model using these two variables generated an R^2 of 0.85 with the *in situ* data in this case, slightly less but comparable to the $\ln SD_{MSI}$ relationship (Fig. 11b):

$$\ln SD_{sOLI} = a_{sOLI}\,(R_{rs}(B2)/R_{rs}(B4)) + b_{sOLI}\,(R_{rs}(B3)) + c_{sOLI} \tag{12}$$

where coefficients a_{sOLI} (2.6758384), b_{sOLI} (−29.49688), and c_{sOLI}

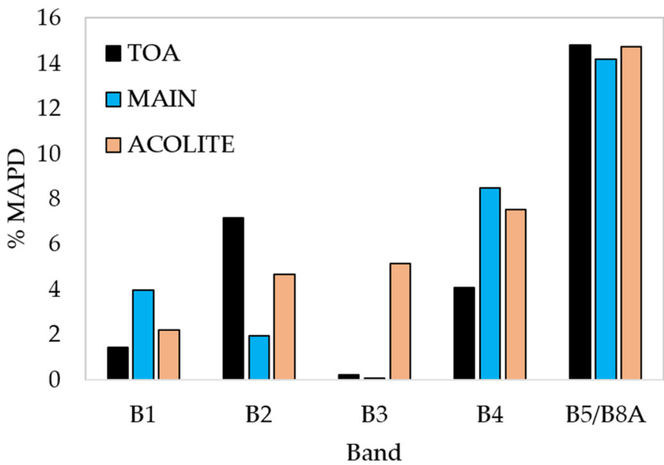

Fig. 8. Mean absolute percent difference (MAPD%) between MSI and OLI reflectance signals before atmospheric correction (TOA) and after MAIN and ACOLITE processing using the coincident 27-Sep 2017 imagery (n = 18).

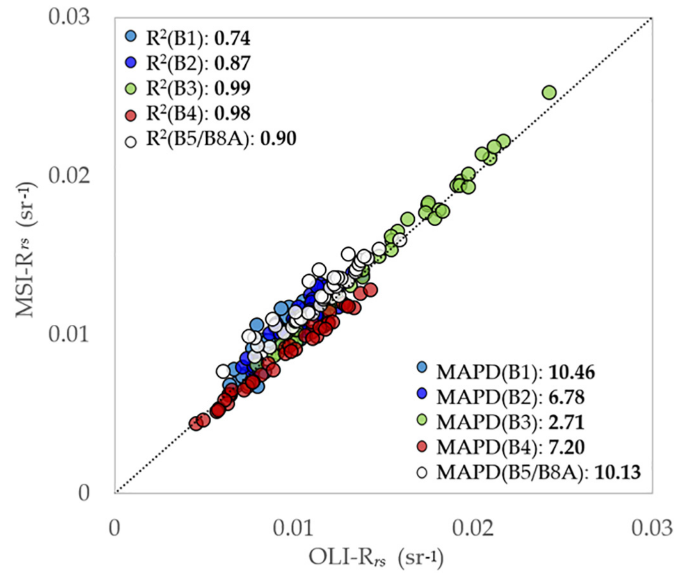

Fig. 10. Harmonized R_{rs} pixel values between MSI (y-axis) and OLI (x-axis) from the coincident overpass imagery acquired on 13-Aug 2018 (n = 43) after MAIN processing.

(-2.468818) were fit to $\ln SD_{sOLI}$ data, and is mainly to be used for MSI in tandem with the OLI sensor after resampling the MSI pixels to match OLI 30 m spatial resolution for future cross-sensor comparisons. Finally, the converted SD_{MSI} and SD_{sOLI} values generated mean absolute errors

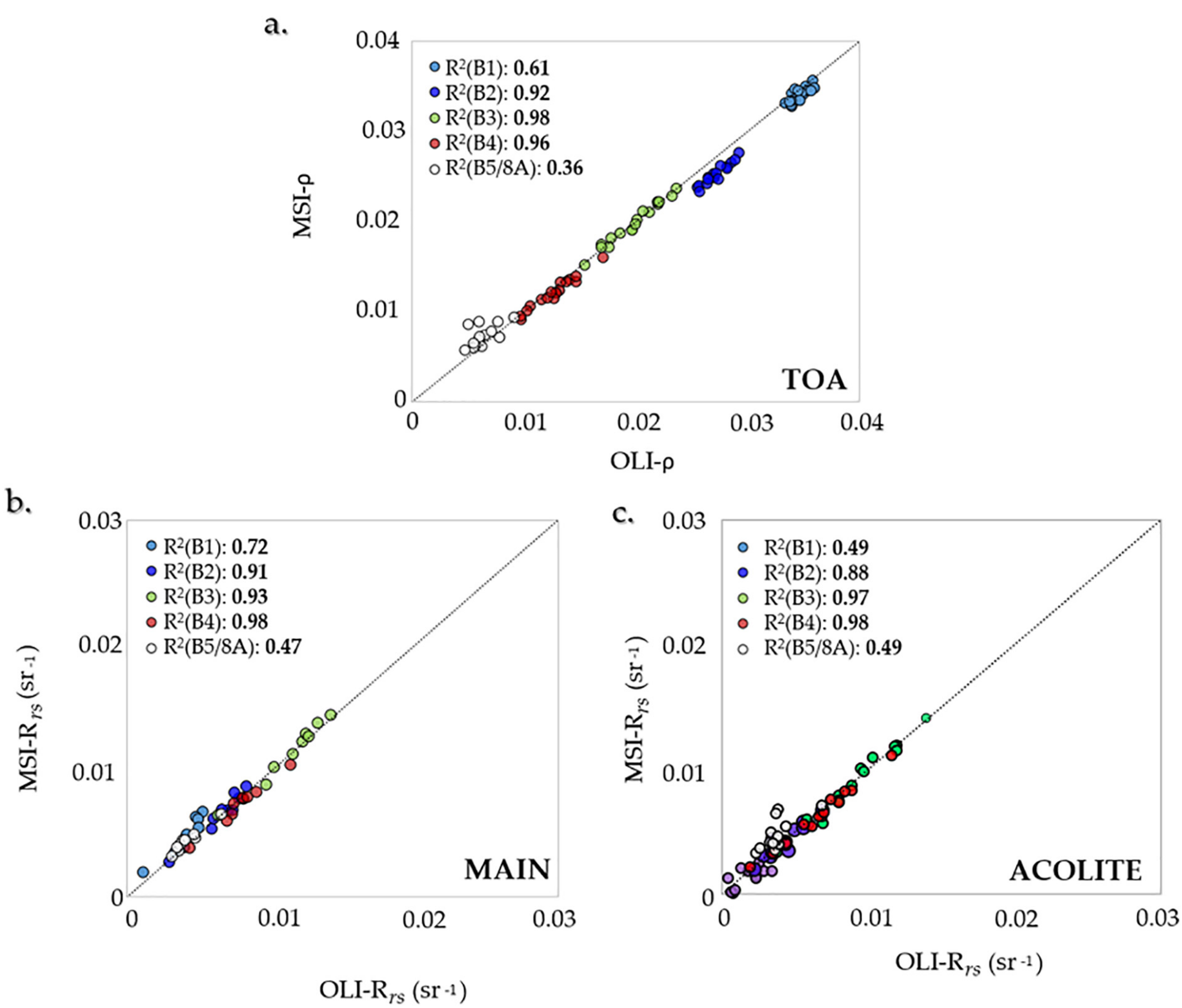

Fig. 9. Band-by-band relationships between comparable MSI (y-axis) and OLI (x-axis) spectral bands before atmospheric correction (TOA) (a) after MAIN (b) and ACOLITE (c) processing using the 27-Sep 2017 coincident overpass imagery (n = 18).

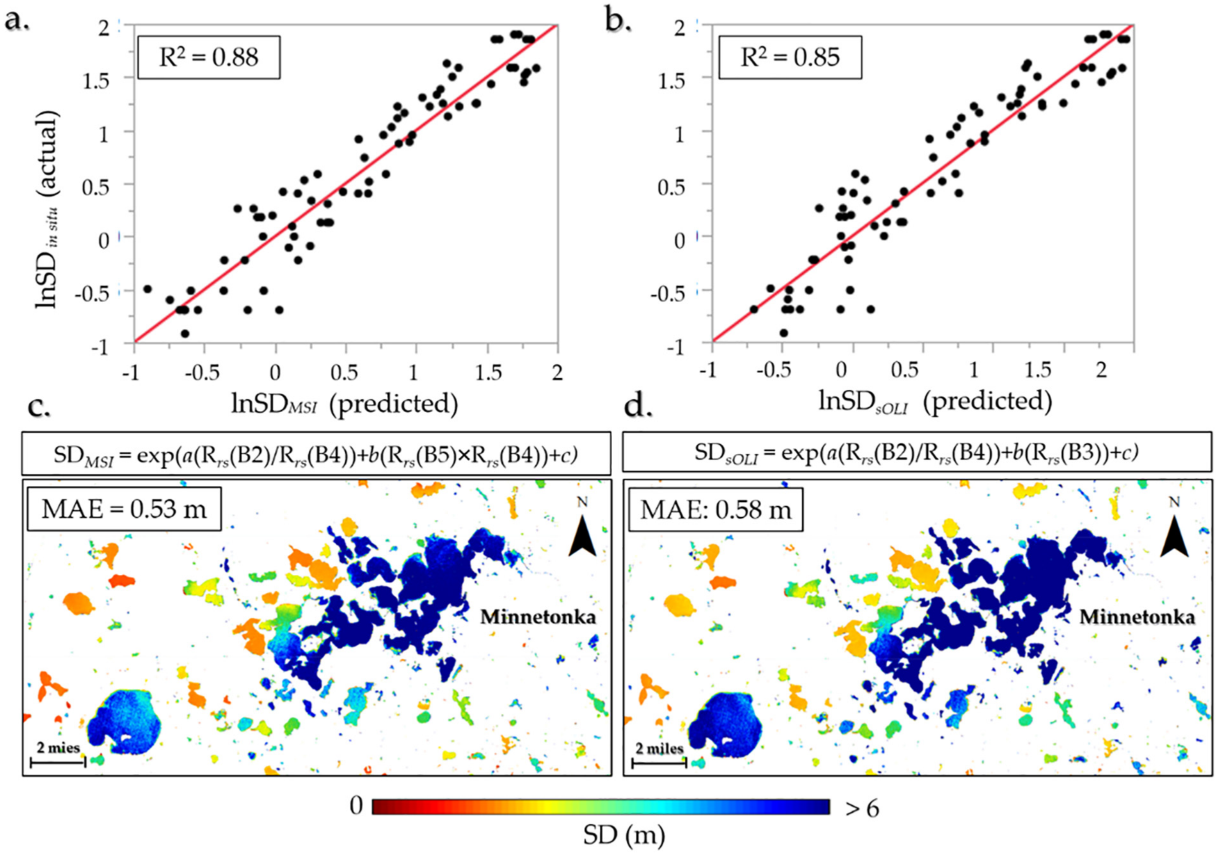

Fig. 11. Performance plots of predicted $\ln SD_{MSI}$ (a) and $\ln SD_{sOLI}$ (b) models against the $\ln SD_{in\ situ}$ calibration dataset from 23-Aug 2017 (n = 79). Corresponding SD maps applied to the 23-Aug 2017 imagery in the GEE API (c).

(MAE) of 0.53 m and 0.58 m against the 23-Aug 2017 calibration dataset, respectively (Fig. 11c and d). This error (in terms of lake management) demonstrates the ability to derive a relatively accurate scene specific map of estimated SD from a MSI or OLI satellite image. For perspective, limnologists usually consider an SD < 2 m as indicative of eutrophic conditions, and SD < 1 m as indicative of hypereutrophy. Next, further validation datasets were used to evaluate whether this MAE varies across different dates of imagery as well as the deviation of the MAE across both sensors (Section 3.3).

3.3. Water clarity model validation

For SD model performance on a temporal scale, we compared three SD datasets corresponding with three dates of imagery: 276 $SD_{in\ situ}$ samples collected by the CLMP corresponding with ± 1 day within a S2A/MSI overpass on 12-Sep 2017 as a primary (1^0) validation dataset (considering the large sample size), 18 samples from the coincident overpass imagery on 27-Sep 2017 (2^0), and 43 samples from a tertiary (3^0) coincident overpass event between MSI and OLI on 13-Aug 2018 described in Section 2.6 (Table 2). The 1^0 validation dataset was mainly used for SD_{MSI} and SD_{sOLI} model consistency for the MSI based models whereas the 2^0 and 3^0 datasets were used to evaluate cross sensor performance between SD_{sOLI} and SD_{OLI} in addition to model validation.

The 1^0 validation dataset (12-Sep 2017) resulted in a MAE only 0.13 m greater than the calibration dataset between SD_{MSI} and $SD_{in\ situ}$ with an MAE of 0.66 m using Eq. (11) (Table 3). Similarly, a comparable MAE of 0.67 m resulted when using the SD_{sOLI} model (Eq. (12)) (a 0.09 m increase from the calibration dataset). The slight increase of MAE using the 1^0 dataset may be a result of the increased sample size compared to the calibration dataset (n = 276) and may indicate a more robust representation of the model error. On the other hand, lower

Table 3
Mean absolute error (MAE) of satellite derived SD estimates from the three validation datasets.

Date	Model	MAE (m)	n
12-Sep-17	SD_{MSI}	0.66	276
	SD_{sOLI}	0.67	
27-Sep-17	SD_{MSI}	0.25	18
	SD_{sOLI}	0.33	
	SD_{OLI}	0.36	
13-Aug-18	SD_{MSI}	0.38	43
	SD_{sOLI}	0.62	
	SD_{OLI}	0.44	

errors resulted when using the cross-sensor model (Eq. (12)) on the 2^0 and 3^0 validation datasets (Table 3). For the 2^0 validation dataset (n = 18), a consistent estimate of SD was generated for both sensors, with MAE of 0.33 m for SD_{sOLI} and 0.36 m for SD_{OLI}, as expected due to the harmonized R_{rs} input bands. When applying Eq. (11) to the MSI imagery, a lower MAE of 0.25 m was generated, reassuring the improvement of water clarity estimation using the 705 nm band. A lower MAE of 0.38 m also resulted in the 3^0 validation dataset when using the SD_{MSI} model opposed to 0.62 m when using SD_{sOLI}. In summary, the developed SD models had a MAE range of 0.25–0.67 m.

Satellite and field measurements can never exactly match. Any disagreements between the two could originate from many sources: difference in spatial coverage (20-30 m pixels *vs.* a single Secchi diameter), error in field measurements, error in the satellite atmospheric correction, and errors in the SD model. Maybe it is more important to look at the consistency of satellite-based values as if they were the standard way of measuring water clarity (*e.g.*, in terms of consistency between sensors, *etc.*) rather than by comparing to ground-based SD values as though they represent the "true values" of water clarity. The relative consistency of MAE values across all three comparisons (1°, 2°, 3°) may be saying something more important than the actual comparisons with the ground data.

4. Conclusions

This study aimed to provide a multi-sensor processing methodology for MSI and OLI imagery to map water clarity in Minnesota so that regional water quality assessments may be carried out in a fast, routine manner. The performance of MAIN was successfully demonstrated as a viable alternative to derive realistic R_{rs} values for lake water quality applications, and the advantage of GEE allows for quick and vigorous testing of the proposed methodologies for both atmospheric correction and water clarity model validation in either different geographical regions or scales.

Implementing the strategies demonstrated in this study in a high performance computing environment will allow the processes to be automated for generating near real-time water clarity maps for Minnesota's inland water bodies as soon as the image products become available for download. The cross-sensor image processing methodology in its current form could have a large impact on the routine monitoring protocols conducted by lake management and other resource agencies. For example, the exported water clarity maps from GEE can readily be implemented into a GIS or other web map service, and could help educate resource managers regarding areas susceptible to eutrophication either in person or online. Further, information derived from these maps could aid in characterizing the phenology of water clarity patterns on a regional scale. Being able to prioritize sampling efforts toward the more affected water bodies without extensive field sampling could become a capacity building exercise for a routine monitoring practice standard, and ultimately reduce time and financial constraints.

Acknowledgements

Support for this research was provided by the University of Minnesota Water Resources Center in cooperation with the U.S. Geological Survey Water Resources Research Act Program and the Minnesota Environment and Natural Resources Trust Fund (ENRTF) through the Legislative-Citizen Commission on Minnesota Resources (LCCMR). Partial support was provided by the National Science Foundation, United States (NSF) award no. 1442672. Sentinel-2 and Landast-8 data were provided by the European Space Agency and USGS, respectively, acquired through the Google Earth Engine JavaScript API. We also thank Pamela Anderson Supervisor of the Water Quality Monitoring Unit, MPCA and the CLMP volunteers for the SD data.

References

Augusto-Silva, P., Ogashawara, I., Barbosa, C., De Carvalho, L., Jorge, D., Fornari, C., Stech, J., 2014. Analysis of MERIS reflectance algorithms for estimating chlorophyll-a concentration in a Brazilian reservoir. Remote Sens. 6, 11689–11707. https://doi.org/10.3390/rs61211689.

Bailey, S., Franz, B., Werdell, J., 2010. Estimation of near-infrared water-leaving reflectance for satellite ocean color data processing. Opt. Express 18, 7521–7527. https://doi.org/10.1364/OE.18.997521.

Bernardo, N., Fernanda, W., Rodrigues, T., Alcantara, E., 2017. Atmospheric correction issues for retrieving total suspended concentrations in inland waters using OLI/Landsat-8 image. Adv. Space Res. 59, 2335–2348. https://doi.org/10.1016/j.asr.2017.02.017.

Bossenbroek, J., Kraft, C., Nekola, J., 2001. Prediction of long-distance dispersal using gravity models: zebra mussel invasion of inland lakes. Ecol. Appl. 11, 1778–1788. https://doi.org/10.1890/1051-0761(2001)011[1778:POLDDUJ2.0.CO;2.

Breiman, L., 1996. Bagging predictors. Mach. Learn. 24 (2), 123–140 (f).

Brezonik, P., Bouchard Jr., R., Finlay, J., Griffin, C., Anderson, J., Arnold, W., Hozalski, R., 2019. Color, chlorophyll a, and suspended solids effects on Secchi depth in lakes: implications for trophic state assessment. Ecol. Appl. 29 (3), e01871 (10/1002/eap.1871).

Carpenter, D., and Carpenter, S. 1983. Modeling inland water quality using Landsat data. Remote Sens. Environ. 13, 345–252. doi:https://doi.org/10.1016/0034-4257(83)90035-4.

Claverie, M., Ju, J., Masek, J.G., Dungan, J., Vermote, E., Roger, J.-C., Skakun, S., Justice, C., 2018. The harmonized Landsat and Sentinel-2 surface reflectance data set. Remote Sens. Environ. 219, 145–161.

Dash, P., Walker, N., Mishra, D., Eurico, D., Ladner, S., 2012. Atmospheric correction and vicarious calibration of Oceansat-1 Ocean Color Monitor (OCM) data in coastal case 2 waters. Remote Sens. 4, 1716–1740. https://doi.org/10.3390/rs4061716.

Doerffer, R., 1992. Imaging Spectroscopy for Detection of Chlorophyll and Suspended Matter. GKSS-Forschungszentrum.

Farr, T., et al., 2007. The shuttle radar topography mission. Rev. Geophys. 45. https://doi.org/10.1029/2005RG000183.

Giardino, C., Pepe, M., Alessandro Brivio, P., Ghezzi, P., Zilioli, E., 2001. Detecting chlorophyll, secchi disk depth and surface temperature in a sub-alpine lake using Landsat imagery. Sci. Total Environ. 268, 19–29. https://doi.org/10.1016/S0048-9697(00)00692-6.

Gitelson, A., Schalles, J., Hladik, C., 2007. Remote chlorophyll-a retrieval in turbid, productive estuaries: Chesapeake Bay case study. Remote Sens. Environ. 109, 464–472. https://doi.org/10.1016/j.rse.2007.01.016.

Gitelson, A., Gurlin, D., Moses, W., and Barrow, T., 2009. A bio-optical algorithm for the remote estimation of the chlorophyll-a concentration in case 2 waters. Environ. Res. Lett. 4 (2009) 045003 (5pp). doi:https://doi.org/10.1088/1748-9326/4/4/045003.

Gordon, H., Wang, M., 1994. Retrieval of water-leaving radiance and aerosol optical thickness over the oceans with SeaWiFS: a preliminary algorithm. Appl. Opt. 33, 443–452. https://doi.org/10.1364/AO.33.000443.

Gordon, H., Clark, D., Brown, J., Brown, O., Evans, R., Broenkow, W., 1983. Phytoplankton pigment concentrations in the middle Atlantic bight: comparison of ship determinations and CZCS estimates. Appl. Opt. 22, 20–36. https://doi.org/10.1364/AO.22.000020.

Gordon, H., Du, T., Zhang, T., 1997. Atmospheric correction of ocean color sensors: analysis of the effects of residual instrument polarization sensitivity. Appl. Opt. 36, 6938–6948. https://doi.org/10.1364/AO.36.006938.

Gorelick, N., Hancher, M., Dixon, M., Ilyushchenko, S., Thau, D., Moore, R., 2017. Google earth engine: planetary-scale geospatial analysis for everyone. Remote Sens. Environ. 202, 18–27. https://doi.org/10.1016/j.rse.2017.06.031.

Hansen, J., Travis, D., 1974. Light scattering in planetary atmospheres. Space Sci. Rev. 16, 527–610. https://doi.org/10.1007/BF00168069.

Harrington, J., Schiebe, F., 1992. Remote sensing of Lake Chicot, Arkansas: monitoring suspended sediments, turbidity, and secchi depth with Landsat MSS data. Remote Sens. Environ. 39, 15–27. https://doi.org/10.1016/0034-4257(92)90137-9.

Hastie, T.J., Tibshirani, R.J., Friedman, J.H., 2009. The Elements of Statistical Learning: Data Mining, Inference, and Prediction, 2nd ed. Springer-Verlag, New York.

Hu, C., Carder, K., Muller-Karger, F., 2000. Atmospheric correction of SeaWiFS imagery over turbid coastal waters: a practical method. Remote Sens. Environ. 7, 195–206. https://doi.org/10.1016/S0034-4257(00)0080-8.

Hu, C., Chen, Z., Clayton, T.D., Swarzenski, P., Brock, J.C., Muller-Karger, F.E., 2004. Assessment of estuarine water-quality indicators using MODIS medium-resolution bands: initial results from Tampa Bay, FL. Remote Sens. Environ. 93, 423–441. https://doi.org/10.1016/j.res.2004.08.007.

Ilori, C.O., Pahlevan, N., Knudby, A., 2019... Analyzing Performances of Different Atmospheric Correction Techniques for Landsat 8: Application for Coastal Remote Sensing. Remote. Sens. 11 (4), 469.

Kloiber, S., Brezonik, P., Olmanson, L., Bauer, M., 2002a. A procedure for regional lake water clarity assessment using Landsat multispectral data. Remote Sens. Environ. 82, 38–47.

Kloiber, S., Brezonik, P., Bauer, M., 2002b. Application of Landsat imagery to regional-scale assessments of lake clarity. Water Res. 36, 4330–4340. https://doi.org/10.1016/S0043-1354(02)00146-X.

Koontz, A., Flynn, C., Hodges, G., Michalsky, J., Barnard, J., 2013. Aerosol Optical Depth Value-Added Product. U.S. Department of Energy, pp. 32.

Kuhn, C., Valerio, A., Ward, N., Loken, L., Sawakuchi, H.O., Kampel, M., Richey, J., Stadler, P., Crawford, J., Striegl, R., Vermote, E., Pahlevan, N., Butman, D., 2019. Performance of Landsat-8 and Sentinel-2 surface reflectance products for river remote sensing retrievals of chlorophyll-a and turbidity. Remote Sens. of Environ. 224, 104–118. https://doi.org/10.1016/j.rse.2019.01.023.

Landsat 8 Data User's Manual. Version 2.0. https://landsat.usgs.gov/sites/default/files/documents/Landsat8DataUsersHandbook.pdf

Lee, Z., Shang, S., Hu, C., Du, K., Weidemann, A., Hou, W., Lin, J., Lin, G., 2016. Secchi disk depth: a new theory and mechanistic model for underwater visibility. Remote Sens. Environ. 169, 139–149. https://doi.org/10.1016/j.rse.2015.08.002.

Lillesand, T.M., 1983. Issues surrounding the commercialization of civil land remote sensing from space. Photogramm. Eng. Remote. Sens.

Mandanici, E., and Bitelli, G., 2016. Preliminary comparison of Sentinel-2 and Landsat-8 imagery for a combined use. Remote Sens., 1014. doi.org/https://doi.org/10.3390/rs8121014.

Markert, K., et al., 2018. Historical and operational monitoring of surface sediments in the Lower Mekong Basin using Landsat and Google Earth Engine cloud computing. Remote Sens. 10, 909.

Mishra, D., Narumalani, S., Rundquist, D., Lawson, M., 2005. Characterizing the vertical diffuse attenuation coefficient for downwelling irradiance in coastal waters: implications for water penetration by high resolution satellite data. ISPRS J. Photogramm. Remote Sens. 60, 48–64. https://doi.org/10.1016/j.isprs.2005.09.003.

Mishra, D., Mishra, R., Lee, Z., and Tucker, C., 2013. Quantifying cyanobacterial phycocyanin concentration in turbid productive waters: a quasi-analytical approach. Remote Sens. Environ. 113, 141–151. doi.org/https://doi.org/10.1016/j.rse.2013.

02.004.
Ogashawara, I., Mishra, D., Gitelson, A., 2017. Remote sensing of inland waters: Background and current state-of-the-art. In: Mishra, D.R., Ogashawara, I., Gitelson, A.A. (Eds.), Bio-Optical Modeling and Remote Sensing of Inland Waters, 1st edition. Elsevier, Waltham, MA, 9780128046449, pp. 332. https://doi.org/10.1016/B978-0-12-804644-9.00001-X.
Olmanson, L., Kloiber, S., Bauer, M., Brezonik, P., 2001. Image Processing Protocol for Regional Assessments of Lake Water Quality. Water Resources Center and Remote Sensing Laboratory, University of Minnesota, St. Paul, MN.
Olmanson, L., Bauer, M., Brezonik, P., 2008. A 20-year Landsat water clarity census of Minnesota's 10,000 lakes. Remote Sens. Environ. 112, 4086–4097. https://doi.org/10.1016/j.rse.2007.12.013.
Olmanson, L., Brezonik, P., Bauer, M., 2013. Geospatial and temporal analysis of a 20-year record of Landsat-based water clarity in Minnesota's 10,000 lakes. Journal of American Water Resources Association 1–14. https://doi.org/10.1111/jawr.12138.
Olmanson, L.G., Brezonik, P.L., Finlay, J.C., Bauer, M.E, 2016. Comparison of Landsat 8 and Landsat 7 for regional measurements of CDOM and water clarity in lakes. Remote Sens. Environ. 185, 119–128.
Olmanson, L., Brezonik, P., and Bauer, M., 2015. Remote sensing for regional lake water quality assessment: capabilities and limitations of current and upcoming satellite systems. *In* Advances in Watershed Science and Assessment, 111–140. doi.org/https://doi.org/10.1007/978-3-319-14212-8_5.
Omernik, J., 1987. Ecoregions of the conterminous United States. Ann. Assoc. Am. Geogr. 77 (1), 118–125.
O'Reilly, C., et. al., 2015. Rapid and highly variable warming of lake surface waters around the globe. AGU Geophysical Research Letters 42, 24. doi:https://doi.org/10.1002/2015GL066235.
Page, B., Kumar, A., and Mishra, D., 2018. A novel cross-satellite based assessment of the spatio-temporal development of a cyanobacterial harmful algal bloom. Int. J. Appl. Earth Obs. Geoinf. 66, 68–81. doi.org/https://doi.org/10.1016/j.jag.2017.11.003.
Pahlevan, N., Schott, J., Franz, B.A., Zibordi, G., Markham, B., Bailey, S., Schaaf, C., Ondrusek, M., Greb, S., Strait, C., 2017a. Landsat 8 remote sensing reflectance (R_{rs}) products: evaluations, intercomparisons and enhancements. Remote Sens. Environ. 190 (1), 289–301. https://doi.org/10.1016/j.rse.2016.12.030.
Pahlevan, N., Sarkar, S., Franz, B.A., Balasubramanian, S.V., and He, J., 2017b. Sentinel-2 MultiSpectral instrument (MSI) data processing for aquatic science applications: demonstrations and validations. Remote Sens. Environ. 201, 47–56. doi.org/https://doi.org/10.1016/j.rse.2017.08.033.
Pahlevan, N., Chittimalli, S., Balasubramanian, S., Vellucci, V., 2019. Sentinel-2/Landsat-8 product consistency and implications for monitoring aquatic systems. Remote Sens. Environ. 220, 19–29. https://doi.org/10.1016/j-rse.2018.10.027.
Seegers, B., Stumpf, R., Schaeffer, B., Loftin, K., Werdell, J., 2018. Performance metrics for the assessment of satellite data products: an ocean color case study. Opt. Express 26 (6), 7404–7422. https://doi.org/10.1364/OE.26007404.
Slonecker, E. T., Jones, D., and Pellerin, B., 2016. The new Landsat 8 potential for remote sensing of colored dissolved organic matter (CDOM). Mar. Pollut. Bull. 107, 2, 518–527. doi.org/https://doi.org/10.1016/j.marpolbul.2016.02.076.
Smith, V., 2016. Effects of eutrophication on maximum algal biomass in lake and river ecosystems. Inland Waters 6, 147–154. doi.org/105268/IW-6.2.937.
Stadelmann, T., Brezonik, P., and Kloiber, S., 2001. Seasonal patterns of chlorophyll-a and Secchi disk transparency in lakes of east-central Minnesota: implications for design of ground- and satellite-based monitoring programs. Lake and Reservoir Management 17, 299–314. doi.org/https://doi.org/10.1080/07438140109354137.
Storey, J., Roy, D., Masek, J., Gascon, F., Dwyer, J., and Choate, M., 2016. A note on the temporary misregistration of Lansdat-8 operational land imager (OLI) and Sentinel-2 multi spectral instrument (MSI) imagery. Remote Sens. Environ. 186, 121–122. doi.org/https://doi.org/10.1016/j.rse.2016.08.025.
Suresh, T., Desa, E., Mascarenhas, A., Matondkar, S., Naik, P., Nayak, S., 2006. Cross-calibration of IRS-P4 OCM satellite sensor. Proc. SPIE 6404, 1–9. https://doi.org/10.1117/12.694019.
Tyler, A., Hunter, P., Spyrakos, E., Groom, S., Maria Constantinescu, A., and Kitchen, J., 2016. Developments in Earth observation for the assessment and monitoring of inland, transitional, coastal and shelf-sea waters. Sci. Total Environ. 572, 1307–1321. doi.org/https://doi.org/10.1016/j.scitotenv.2016.01.020.
Vanhellemont, Q., and Ruddick, K., 2014. Turbid wakes associated with offshore wind turbines observed with Landsat 8. Remote Sens. Environ. 145, 105–115. doi.org/https://doi.org/10.1016/j.rse.2014.01.009.
Vanhellemont, Q., and Ruddick, K., 2015. Advantages of high quality SWIR bands for ocean colour processing: examples from Landsat-8. Remote Sens. Environ. 161, 89–106. doi.org/https://doi.org/10.1016/j.rse.2015.02.007.
Vanhellemont, Q., Ruddick, K., 2016. Acolite for Sentinel-2: Aquatic applications of MSI imagery. In: Proceedings of the 2016 ESA Living Planet Symposium. ESA Special Publication, SP, pp. 740.
Vermote, E., Justice, C., Claverie, M., and Franch, B., 2016. Preliminary analysis of the performance of the Landsat 8/OLI land surface reflectance product. Remote Sens. Environ. 185, 46–56. doi.org/https://doi.org/10.1016/j.rse.2016.04.008.
Wang, M., Son, S., Shi, W., 2009. Evaluation of MODIS SWIR ad NIR-SWIR atmospheric correction algorithms using SeaBASS data. Remote Sens. Environ. 113, 635–644.
Watanabe, F., Alcantara, E., Rodrigues, T., Imai, N., Barbosa, C., and da Silva Rotta, L., 2015. Estimation of chlorophyll-aconcentration and the trophic state of the Barra Bonita hydroelectric reservoir using OLI/Landsat-8 images. Int. J. Environ. Res. Public Health, 12, 10391–10417. doi.org/https://doi.org/10.3390/ijerph120910391.
Werdell, J., Franz, B., Bailey, S., 2010. Evaluation of shortwave infrared atmospheric correction for ocean color remote sensing of Chesapeake Bay. Remote Sens. Environ. 114, 2238–2247. https://doi.org/10.1016/j.rse.2010.04.027.